Preprints (www.preprints.org) | NOT PEER-REVIEWED | Posted: 9 August 2022 doi:10.20944/preprints202208.0170.v1

Article

Impact of Astrocytic Coverage of Synapses on the Short-term Memory of a Computational Neuron-Astrocyte Network

Zonglun Li[1,2], Yuliya Tsybina[3], Susanna Gordleeva[3,5] and Alexey Zaikin[1,2,3,4]*

[1] Department of Mathematics, University College London, London, United Kingdom
[2] Institute for Women's Health, University College London, London, United Kingdom
[3] Lobachevsky State University of Nizhny Novgorod, Nizhny Novgorod, Russia
[4] World-Class Research Center "Digital Biodesign and Personalized Healthcare", Sechenov University, Moscow 119991, Russia
[5] Samara Medical University, Samara, Russia
* Correspondence: alexey.zaikin@ucl.ac.uk

Abstract: Working memory refers to the capability of the nervous system to selectively retain short-term memories in an active state. The long-standing viewpoint is that neurons play an indispensable role and working memory is encoded by synaptic plasticity. Furthermore, some recent studies have shown that calcium signaling assists the memory processes and the working memory might be affected by the astrocyte density. Over the last few decades, growing evidence has also revealed that astrocytes exhibit diverse coverage of synapses which are considered to participate in neuronal activities. However, very little effort has yet been made to attempt to shed light on the potential correlations between these observations. Hence, in this article we will leverage a computational neuron-astrocyte model to study the short-term memory performance subject to various astrocytic coverage and we will demonstrate that the short-term memory is susceptible to this factor. Our model may also provide plausible hypotheses for the various sizes of calcium events as they are reckoned to be correlated with the astrocytic coverage.

Keywords: neuron; astrocyte; network; short-term memory; spatial frequency; computational biology

1. Introduction

Over the past few decades, increasing effort has been devoted to understanding the roles played by a type of glial cells, astrocytes [1–6]. Traditionally, astrocytes have been reckoned as auxiliary cells to neurons and it has now become evident that astrocytes can not only support the structure of the nervous system, but also modulate synaptic transmission [7–11]. Neuron-astrocyte coupling plays an indispensable role in the functioning of neuronal networks via bidirectional communication under the notion 'tripartite synapse' [12–16]. It is found that astrocytes can sense the synaptic activities by the uptake of neurotransmitters released from the synaptic cleft and provide feedback to pre- and post-synaptic neurons via gliotransmitter release caused by temporary elevation of intracellular calcium concentration which normally lasts seconds to minutes [17–19,22,31]. All these findings in molecular biology pave the way for a better understanding of the information processing in neuron-astrocyte circuits and the formation of cognitive functions. Very recently, mathematical and computational approaches have been used to investigate the contribution of astrocytes to the organisation of spatial and temporal synchronization in neural networks [20,21,29,30], formation of short-term memory [23–28] and generation of integrated information in neuronal ensembles [32–35], which takes a step further to the understanding of the intelligence arising from the nervous system.

Nowadays, a widely accepted fact is that astrocytes play an active role in various types of memory and the memory improvement may be related to changes in the astrocyte density [36–40]. Working memory is the ability of an entity to retain limited information

 doi:10.20944/preprints202208.0170.v1

in a readily accessible form and provides an interface between memory and cognition [41–43]. Some biological evidence has already raised the possibility that astrocytes could be highly involved in working memory [44–47] and it has been well known that the astrocytic coverage of synapses is a highly dynamic process that alters throughout lifetime [48–50]. Therefore, it is natural to hypothesize that there exists a potential correlation between the working memory and the astrocytic coverage (or astrocyte density) but very little effort has been made so far. In this work, the astrocytic coverage is equivalent to the astrocyte density and it will become clear when we introduce our model. Furthermore, some studies have also revealed that the attenuation of calcium events correlates with the reduction of astrocytic coverage of asymmetric synapses in the hippocampal CA1 region in mice and that the size of the calcium events within astrocytes follow power law distributions [51–54]. Hence, this line of research may also help explain the cause of various sizes of calcium events.

Lately, an *in silico* neuron-astrocyte network model has been employed to manifest that astrocytes indeed assist the formation of short-term memory and mediate analogous memory [24–28]. It provides a quantitative score to measure the recall accuracy as a result of the short-term memory. In this work, we will leverage this computational model and study the impact of varying astrocytic coverage areas of synapses on the short-term memory performance. Unlike in the original article [25], here we focus on the performance of the single-item task so as to ensure that the real pattern remains unchanged throughout the experiment. We also introduced a low-pass filter to the input image in order to alter the spatial frequencies. In particular, it is of great interest to learn how the change in the number of spatial frequency components will impact the short-term memory and how the relation is affected by the astrocytic coverage. The input image is also subject to different levels of the salt-and-pepper noise to make our evaluation more comprehensive. We will demonstrate that the short-term memory performance is significantly affected by the astrocytic coverage. Additionally, we will also underlie some other observations that may interest biologists.

2. Models and Methods

Our work employed the neuron-astrocyte network developed in [25] and an illustrative diagram for the architecture is shown in Figure 1. From left to right are the input image, neuronal network and astrocytic network, respectively. The neuronal network is of dimension $W \times W$ and the astrocytic network is of dimension $M \times M$. All the neurons are excitatory neurons and each astrocyte from the astrocytic network regulates an $l \times l$ neuronal square from the neuronal network. The connections in the neuronal network will be defined later and the astrocytes in the astrocytic layer are connected to their nearest neighbours vertically and horizontally. The input digital image is converted into electric current and is applied to the neuronal network in that one image pixel corresponds to exactly one neuron. The values used for the parameters introduced in section 2.1, 2.2 and 2.3 are listed in [25], unless otherwise specified.

Preprints (www.preprints.org) | NOT PEER-REVIEWED | Posted: 9 August 2022 doi:10.20944/preprints202208.0170.v1

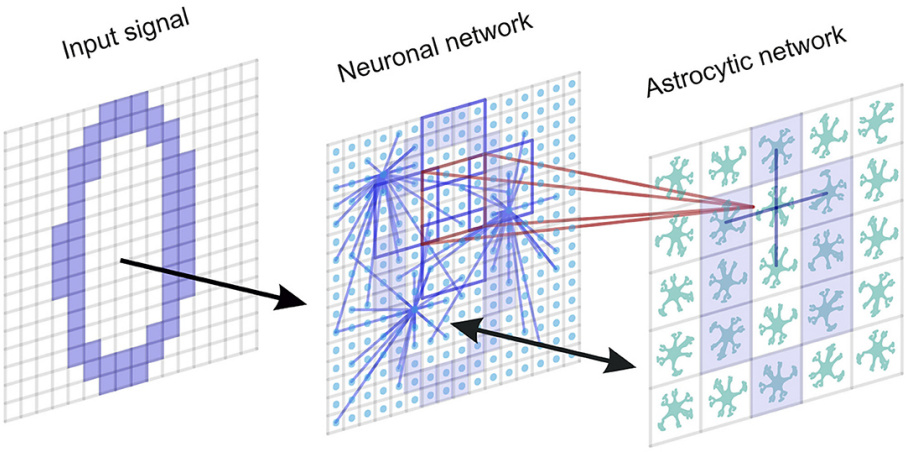

Figure 1. An illustrative diagram for the neuron-astrocyte network [25].

2.1. Neuronal Network

Considering we will be simulating a relatively large network, we use the Izhikevich model to characterize the dynamics of neurons as it demonstrates computational efficiency while maintaining the biological plausibility of the canonical Hodgkin-Huxley model [55]:

$$\begin{cases} \dfrac{dV^{(i,j)}}{dt} = 0.04V^{(i,j)^2} + 5V^{(i,j)} - U^{(i,j)} + 140 + I_{app}^{(i,j)} + I_{syn}^{(i,j)} \\ \dfrac{dU^{(i,j)}}{dt} = a(bV^{(i,j)} - U^{(i,j)}) \end{cases} \tag{1}$$

where V denotes the membrane potential of the particular neuron and U represents the membrane recovery variable, with post-spike resetting: if $V^{(i,j)} \geq 30mV$, then

$$\begin{cases} V^{(i,j)} = c \\ U^{(i,j)} = U^{(i,j)} + d \end{cases} \tag{2}$$

The superscript (i,j) denotes the positional index of the neuron. I_{app} represents the applied input current converted from the digital image and I_{syn} represents the net current receiving from all presynaptic neurons which takes the form (generalized from [56,57]):

$$I_{syn}^{(i,j)} = \sum_k \frac{g_{syn}^{(i,j)}(E_{syn} - V^{(i,j)})}{1 + \exp\left(\frac{-V_{pre}^k}{k_{syn}}\right)} \tag{3}$$

where the summation is over all presynaptic neurons. The synaptic weight is dictated by $g_{syn}^{(i,j)} = \eta + \nu^{(i,j)}$ where η reflects the baseline weight and $\nu^{(i,j)}$ describes the impact of astrocytic calcium events which will be defined later. E_{syn} denotes the reversal potential for excitatory synapses and V_{pre}^k denotes the membrane potential of the neuron k. For clarity, we need to point out that here the short-term synaptic plasticity is not considered in our model. By convention, we use $a = 0.1, b = 0.2, c = -65, d = 2$.

In this work, we fixed the number of out-connections per neuron as N_{out} in that each presynaptic neuron interacts with N_{out} postsynaptic neurons. The connections are established according to an exponential distribution with R being the distance between each pair of neurons:

$$f(R) = \begin{cases} \dfrac{1}{\lambda}\exp(-R/\lambda) & R \geq 0 \\ 0 & R < 0 \end{cases} \tag{4}$$

Preprints (www.preprints.org) | NOT PEER-REVIEWED | Posted: 9 August 2022 doi:10.20944/preprints202208.0170.v1

2.2. Action potential-induced elevation of glutamate and IP_3

For each presynaptic neuron, the amount of glutamate, a type of neurotransmitter released into the synaptic cleft is dictated by the spiking events of the neuron [58]:

$$\frac{dG^{(i,j)}}{dt} = -\alpha_{glu} G^{(i,j)} + k_{glu}\Theta(V^{(i,j)} - 30) \tag{5}$$

where Θ denotes the Heaviside function.

IP_3 is a ligand and is produced in a response to the external stimuli such as neurotransmitters [59]. It regulates many pathways including the release of Ca^{2+} from Endoplasmic Reticulum (ER) into cytoplasm [60] which will be described in due course. The dynamics of intracellular concentration of the molecule IP_3 within each astrocyte is described by

$$\frac{dIP_3^{(m,n)}}{dt} = \frac{IP_3^{\star} - IP_3^{(m,n)}}{\tau_{IP_3}} + J_{PLC_\delta}^{(m,n)} + J_{glu}^{(m,n)} + diff_{IP_3}^{(m,n)} \tag{6}$$

Here $IP_3^{\star}$ denotes the steady state of the intracellular IP_3 concentration and J_{PLC_δ} encapsulates the IP_3 produced by phospholipase $C\delta$ which takes the form

$$J_{PLC_\delta} = \frac{v_4(Ca + (1-\alpha)k_4)}{Ca + k_4} \tag{7}$$

where Ca denotes the Ca^{2+} concentration in the astrocytic cytoplasm. We use $diff_{IP_3}$ to represent the diffusion of IP_3 via gap junctions between adjacent astrocytes and is given by

$$diff_{IP_3} = d_{IP_3}(\Delta IP_3) \tag{8}$$

where ΔIP_3 denotes the discrete Laplace operators reflecting the diffusion as a result of Ca^{2+} exchange with neighbouring astrocytes. The production of IP_3 stimulated by glutamate via metabotropic glutamate receptors (mGluRs) and phospholipase $C\beta$ is characterised by

$$J_{glu} = \begin{cases} A_{glu} & t_0 < t \leq t_0 + t_{glu} \\ 0 & \text{otherwise} \end{cases} \tag{9}$$

where t_{glu} denotes the duration persists since time t_0, when the total level of glutamate associated with a particular astrocyte reaches the threshold F_{act}:

$$\frac{1}{N_a} \sum_{(i,j)\in N_a} \Theta(G^{(i,j)} - G_{thr}) > F_{act} \tag{10}$$

Here we use $t_{glu} = 0.06s$.

2.3. Astrocytic network

Although voltage-gated calcium channels (VGCC) have been shown to be able to elevate intracellular calcium concentration and many authors included them in their models [61–64], here we use the Ullah model [65] to simplify the description of the calcium dynamics within astrocytes where only the impact of glutamate is considered:

$$\begin{cases} \dfrac{dCa^{(m,n)}}{dt} = J_{ER}^{(m,n)} - J_{pump}^{(m,n)} + J_{leak}^{(m,n)} + J_{in}^{(m,n)} - J_{out}^{(m,n)} + diff_{Ca}^{(m,n)} \\ \dfrac{dh^{(m,n)}}{dt} = a_2\left(d_2 \dfrac{IP_3^{(m,n)} + d_1}{IP_3^{(m,n)} + d_3}(1 - h^{(m,n)}) - Ca^{(m,n)} h^{(m,n)}\right) \end{cases} \tag{11}$$

Preprints (www.preprints.org) | NOT PEER-REVIEWED | Posted: 9 August 2022 doi:10.20944/preprints202208.0170.v1

The explicit forms of the individual terms are summarised as below:

$$\begin{cases} J_{ER} = c_1 v_1 Ca^3 h^3 IP_3^3 \dfrac{c_0/c_1 - (1+1/c_1)Ca}{(IP_3+d_1)^3(Ca+d_5)^3} \\ J_{pump} = \dfrac{v_3 Ca^2}{k_3^2 + Ca^2} \\ J_{leak} = c_1 v_2 (c_0/c_1 - (1+1/c_1)Ca) \\ J_{in} = \dfrac{v_6 IP_3^2}{k_2^2 + IP_3^2} \\ J_{out} = k_1 Ca \\ diff_{Ca} = d_{Ca}(\Delta Ca) \end{cases} \tag{12}$$

Here Ca denotes the Ca^{2+} concentration within cytoplasm and h denotes the fraction of opened IP_3 receptors (IP3Rs) on the ER. We assume that the astrocytes are spatially homogeneous. ER is a continuous membrane system that stores a reservoir of Ca^{2+} within astrocytes. The released IP_3 then binds to IP3Rs on the ER and opens the channel allowing for the flow of Ca^{2+} from the ER into the cytoplasm, which is characterised by J_{ER}. In this model, we assume the co-existence of the ER and the cytoplasm in individual astrocytes and the homogeneous distribution of ER in the interior of astrocytes. J_{pump} denotes the ATP-dependent pump recovering Ca^{2+} from the cytoplasm back to the ER. J_{leak} denotes the leakage of Ca^{2+} from the ER to the cytosol due to the concentration gradient. J_{in} and J_{out} denote the Ca^{2+} exchange with the extracellular space. $diff_{Ca}$ represents the diffusion of Ca^{2+} via gap junctions.

Finally, the calcium-dependent gliotransmitter-induced modulation of synaptic weight by the associated astrocyte via the N-methyl-D-asparate receptors (NMDARs) is defined as

$$\nu = \nu^{\star}\Theta(Ca - Ca_{thr}) \tag{13}$$

where $\nu^{\star}$ denotes the weight of the synapse as a result of the astrocytic modulation of synaptic transmission if the Ca^{2+} concentration is beyond the threshold required for gliotransmitter release, Ca_{thr}, and the fraction of spiking neurons associated with that astrocyte during the time interval τ_{syn} is F_{astro}. The duration of feedback is denoted by τ_{astro} and we use $\tau_{astro} = 250ms$.

2.4. Variation of astrocytic coverage

In order to study the working memory performance of the network under various astrocytic coverage areas, we need to vary the size of the astrocytic layer M. However, to ensure that each astrocyte modulates an identical size of neuronal square and there is no leftover neuron, the following equation must be satisfied:

$$\frac{W-1}{l-p} = M \tag{14}$$

where p is the size of the overlapping edge. In this work, we fixed $p = 1$. Since the input image is of dimension 79×79, if $W = 79$, the equation is satisfied for $l = 2, 3, 4, 7$. To analyze the effect of $l = 5, 6, 9$, the image is adjusted by adding a periphery of stripe of width 1 outside of the edge, the intensity of which is chosen to be the same as the background. Now $W = 81$ and the equation is satisfied. Similarly, the equation is satisfied for $l = 8$ by choosing $W = 78$ (edge removal on one side). In this way, the size of the image is by and large maintained and the digital patterns are least damaged.

2.5. Variation of spatial frequencies

In this work, we utilized low-pass filter to alter the spatial frequencies of the input image.

Preprints (www.preprints.org) | NOT PEER-REVIEWED | Posted: 9 August 2022 doi:10.20944/preprints202208.0170.v1

The 2D discrete forward Fourier transform converts the image from the spatial domain into the frequency domain with:

$$F(k,l) = \sum_{x=0}^{W-1} \sum_{y=0}^{W-1} f(x,y) e^{-i2\pi(\frac{kx}{W} + \frac{ly}{W})} \tag{15}$$

The inverse transform converts from the frequency domain back to the spatial domain with:

$$f(x,y) = \frac{1}{W^2} \sum_{k=0}^{W-1} \sum_{l=0}^{W-1} F(k,l) e^{i2\pi(\frac{kx}{W} + \frac{ly}{W})} \tag{16}$$

where $f(x,y)$ denotes the intensity at pixel (x,y) whilst $F(k,l)$ consists of the spectrum and the phase angle at frequency (k,l). In general, one is more concerned with the spectrum as compared to the angle so the angle is not within the scope of our discussion. Figure 2 displays what digit zero looks like in the spatial domain (left) and spectral domain (right) respectively. By convention, the image mean $F(0,0)$ is placed at the center of the spectral domain and is also the largest component of the image. Moreover, we display the frequency domain on the logarithmic scale so as to make the other frequency components more visible. The frequency increases as we move farther away from the center in the spectral domain.

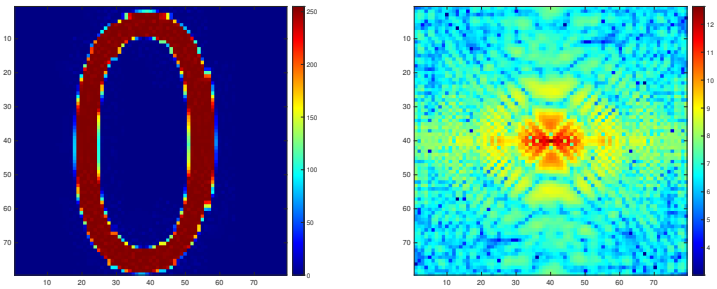

Figure 2. Spatial domain and spectral domain of digit 0.

A low-pass filter applies a threshold f_0 to the spectral domain and set all the components above f_0 to zero. In this work, the filter will be applied to the input current at each time step. By slowly increasing the threshold, we hope to figure out the sensitivity of the short-term memory performance to the change in the spatial frequencies.

2.6. Simulation protocols

Most of the parameter values and protocols used in this work are identical to those used in [25]. Here we only made a few adjustments in order to study the impact of spatial frequencies in a more effective way. Therefore, unless otherwise specified, one can assume we herein use the same protocol as in [25].

The dynamics of the astrocytic network is simulated using the Runge-Kutta fourth-order method and the remaining part using forward Euler method with time-step $\Delta t = 0.1$ms. The input current I_{app} is converted from a digital image (0-9) with the same size of the neuronal network by scaling the pixel intensity, which will be used in the learning and testing stage. The pixel intensity is scaled in the range $[0, A_{stim}]$ for learning and $[0, A_{test}]$ for testing in order to prevent over-excitation of neurons. In this work, we employ the binary encoding that converts intensity over 127 to A_{stim} (A_{test}) and to 0 otherwise. The input is also subject to salt-and-pepper noise which will also alter the frequency domain in addition to the low-pass filter. Different from a low-pass filter which will cut off the frequency components above a threshold, increasing the salt-and-pepper noise tends to increase more frequency components (high frequency components in particular) as the noise will break the image down into pieces. We are interested in investigating the effect of both on the short-term memory performance. In this work, we do not introduce it in the learning stage

Preprints (www.preprints.org) | NOT PEER-REVIEWED | Posted: 9 August 2022 doi:10.20944/preprints202208.0170.v1

to keep the real pattern intact and alter the noise level in the testing stage. Here our work is only focused on the single-item implementation. This is to ensure that the real spatial pattern is fixed during the experiment. Unless otherwise specified, in the learning stage, the input current I_{app} is applied to the network at $t_1 = 0.1$s for $t_{stim} = 200$ms and in the testing stage, I_{app} is applied to the network at $t_2 = 2$s for $t_{test} = 150$ms. The simulation ends at $t_e = 2.3$s. We will alter t_2 and t_e when investigating the impact of the time interval between training and testing. Also note that changing the frequency domain will result in complex values in the spatial domain when conducting the inverse transform. To this end, we take the absolute values and re-scale them with A_{stim} (A_{test}). Our simulation time is shorter as compared to the one used in [25] but the time interval between the learning and the testing stage is already long enough for the activation of calcium release within astrocytes.

2.7. Performance measure

To measure the performance of our model, i.e., to what extent the model is able to memorize the real pattern, we came up with a correlation measure C_p that compares the recalled pattern (during testing) with the real pattern:

$$\begin{cases} M_{ij}(t) = I\left[\left(\sum_{k=t}^{t+\omega} I[V_{ij}(k) > 30]\right) > thr\right] \\ CD(t) = \frac{1}{|P|}\sum_{(i,j)\in P} M_{ij}(t) \\ CB(t) = \frac{1}{W^2 - |P|}\sum_{(i,j)\notin P}(1 - M_{ij}(t)) \\ C(t) = \frac{1}{2}(CD(t) + CB(t)) \\ C_p = \max_{thr} C(t) \end{cases} \tag{17}$$

Here t is the start time of the testing stage and we use $\omega = 250ms$. P represents the set of pixels belonging to the real pattern. CD represents the true positive rate in our context, namely, how many pixels that belong to the real pattern have been recalled. Similarly, CB represents the true negative rate. Therefore, C can accurately reflect the overall performance of the neuron-astrocyte network. We select C_p that maximizes $C(t)$ over the whole-number thresholds, $thr = 1, 2, ..., 30$.

3. Results

In this chapter, we will mainly exhibit how the short-term memory performance is affected by astrocytic coverage under various spatial frequencies and salt-and-pepper noise levels.

Figure 12 and 13 display the model's performance scores C_p for digit zero (a symmetric digit) and two (an asymmetric digit) under various conditions respectively. Each square represents one single simulation using the protocol described in the last chapter. In each sub-figure, the vertical axis denotes various levels of the salt-and-pepper noise at the testing stage. The horizontal axis denotes the moving threshold f_0 (increased by 2 units) of the low-pass filter from $f_0 = 4$ to $f_0 = 58$. Namely, more frequencies will be included as we move farther away from the origin. The plot starting from $f_0 = 4$ is to ensure the visual contrast for the performance over $f_0 = 4$ and we will explain in more details why there exists a sharp rise in performance from 4 later. The filter threshold terminates at $f_0 = 58$ because it will already incorporate all frequency components with respect to the largest picture ($W = 81$) in this study.

On the one hand, for all sizes ($l = 2, 3, 4, 5, 6, 7, 8, 9$) of the astrocytic coverage and noise level during the testing stage, the performance plunges when moving the filter threshold

Preprints (www.preprints.org) | NOT PEER-REVIEWED | Posted: 9 August 2022 doi:10.20944/preprints202208.0170.v1

from 5 to 4, which corresponds to $(5 \times 2)/79 \approx 1/8 - (4 \times 2)/79 \approx 1/10$ of the distance from the center to the edge in the spectral domain. On the other hand, the trace width of the digit in the image we use is about 8-10 pixels. By trace width we mean the interval between the boundaries of the digit. This makes it a wavelength of 16-20 (so a frequency of 1/16-1/20, namely 1/8-1/10 of the distance from the center to the edge in the frequency domain). This correspondence demonstrates that our short-term memory model does manage to detect the dominant frequency pattern of the input image. The performance of the other integer threshold (1,2,3) is not shown in Figure 12 and 13 because we would like to have a contrasting color scale for higher thresholds. As expected, the performance decreases sharply from $f_0 = 4$ to $f_0 = 0$ which is demonstrated in Figure 3. Here the threshold is increased by 1 unit.

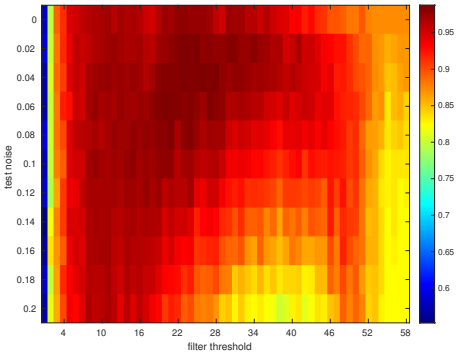

Figure 3. The performance score C_p at diverse levels of noise with $l = 8$ for digit 0 including all the whole-number thresholds.

From Figure 12 and 13, we note that our model is mostly tolerant of noise up to the noise level equal to 0.1. This manifests that our network is able to precisely recall very analogous patterns but have some trouble recalling the exact patterns for less analogous inputs. Another notable feature is that there exists a shift in performance pattern under different filter thresholds as the astrocytic coverage size is increased from $l = 2$ to $l = 9$, and next we will use $l = 4$ and $l = 8$ to explain it at greater length.

From Figure 12 we observe that for $l = 4$, the performance color transitions from red to blue and back to red at a relatively high noise level. Take for example noise level equal to 0.2 (Figure 4), a low filter threshold, $f_0 = 10$ smooths the picture and prevents over-firing of neurons. A high filter threshold, $f_0 = 58$, ensures that most of the digital pixels are firing, although at the cost of a slight over-firing. However, a middle one, $f_0 = 40$ corrupts the picture to a certain degree and yields a relatively low performance. For $l = 8$, the performance color transitions from red to blue and there exists a slight recovery before going down again at high noise levels. At the noise level equal to 0.2 (Figure 5), the firing patterns of $f_0 = 10$ and $f_0 = 40$ are very similar to those in $l = 4$, despite the alteration in the astrocytic coverage. However, for $f_0 = 58$, $l = 8$ significantly favors the over-firing which results in many misclassifications, and $f_0 = 50$ is somewhere in the middle.

Preprints (www.preprints.org) | NOT PEER-REVIEWED | Posted: 9 August 2022 doi:10.20944/preprints202208.0170.v1

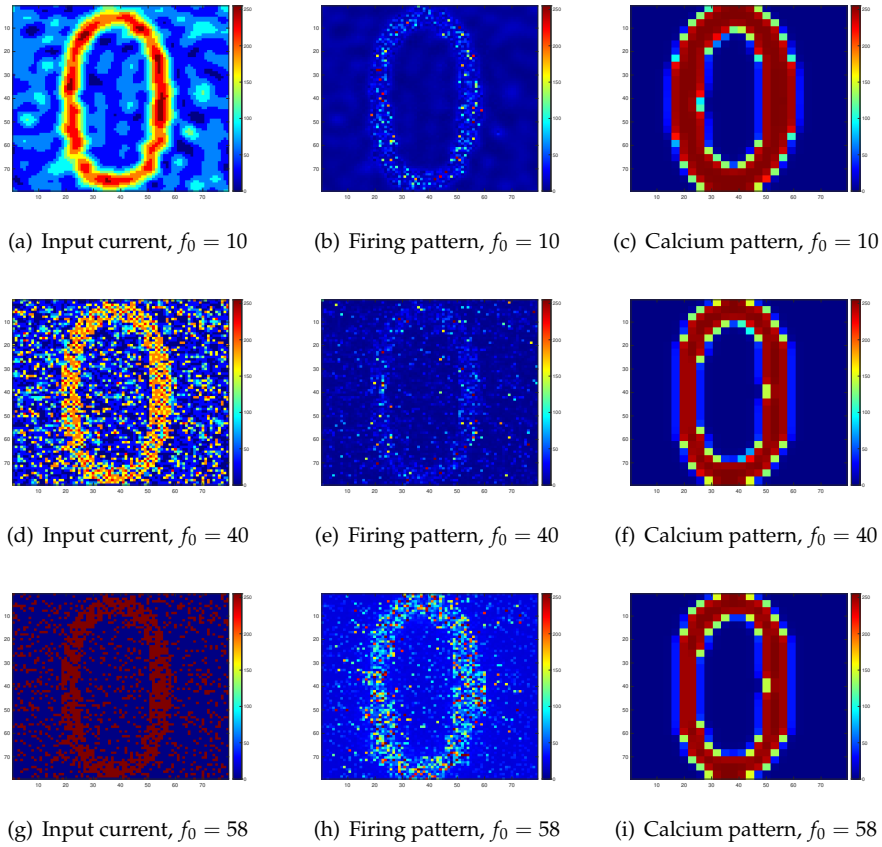

(a) Input current, $f_0 = 10$ (b) Firing pattern, $f_0 = 10$ (c) Calcium pattern, $f_0 = 10$

(d) Input current, $f_0 = 40$ (e) Firing pattern, $f_0 = 40$ (f) Calcium pattern, $f_0 = 40$

(g) Input current, $f_0 = 58$ (h) Firing pattern, $f_0 = 58$ (i) Calcium pattern, $f_0 = 58$

Figure 4. Snapshots for $l = 4$. The left panel displays the input current after being transformed by the low-pass filter at testing. The middle panel displays the firing pattern of neurons at $t = 2.1$s. The right panel displays the calcium pattern of astrocytes at $t = 2$s. The brightness has been scaled in the range 0-255 for visualization.

Preprints (www.preprints.org) | NOT PEER-REVIEWED | Posted: 9 August 2022 doi:10.20944/preprints202208.0170.v1

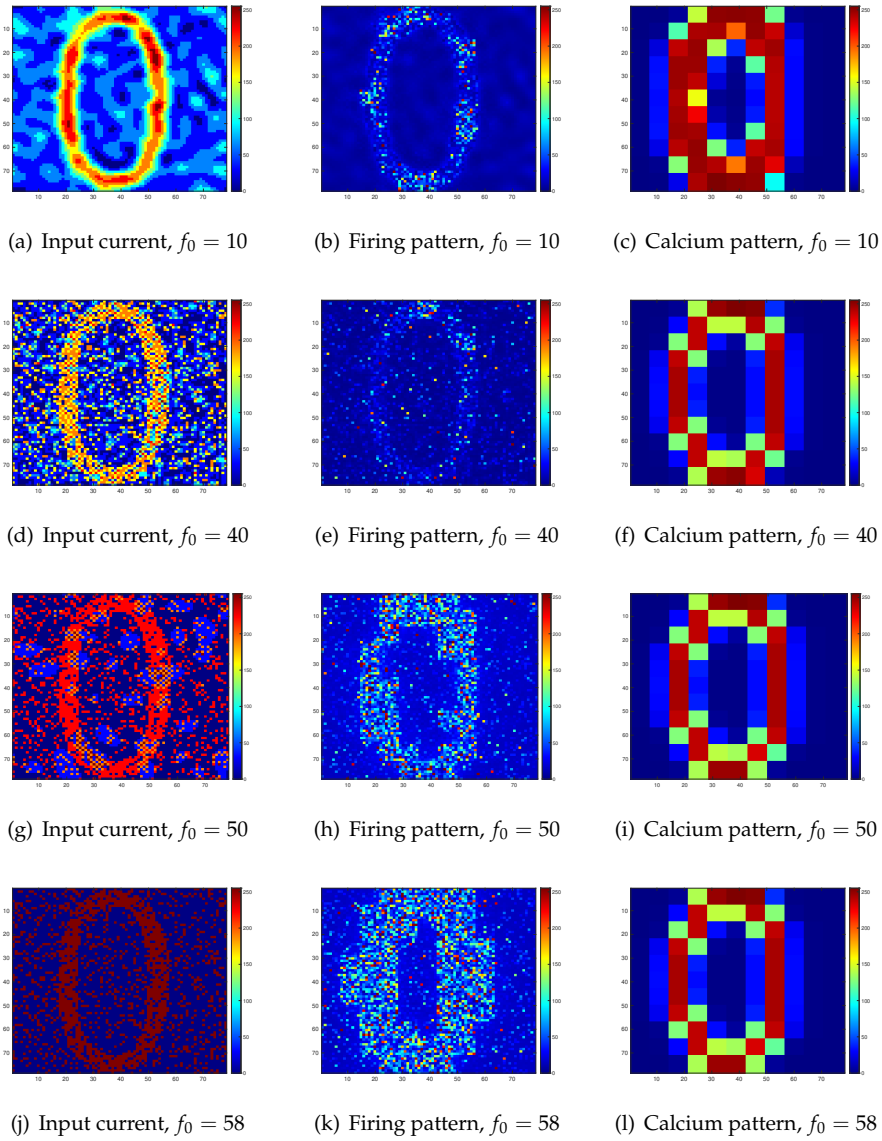

(a) Input current, $f_0 = 10$ (b) Firing pattern, $f_0 = 10$ (c) Calcium pattern, $f_0 = 10$

(d) Input current, $f_0 = 40$ (e) Firing pattern, $f_0 = 40$ (f) Calcium pattern, $f_0 = 40$

(g) Input current, $f_0 = 50$ (h) Firing pattern, $f_0 = 50$ (i) Calcium pattern, $f_0 = 50$

(j) Input current, $f_0 = 58$ (k) Firing pattern, $f_0 = 58$ (l) Calcium pattern, $f_0 = 58$

Figure 5. Snapshots for $l = 8$. The left panel displays the input current after being transformed by the low-pass filter at testing. The middle panel displays the firing pattern of neurons at $t = 2.1$s. The right panel displays the calcium pattern of astrocytes at $t = 2$s. The brightness has been scaled in the range 0-255 for visualization.

In order to better summarize the results shown in Figure 12, we will use box plots to exhibit our statistical analysis. Figure 6(a) displays the overall short-term memory performance subject to low salt-and-pepper noises by grouping the noise level from 0 to 0.1. Similarly, the performance subject to high salt-and-pepper noises is shown in Figure 6(b) by grouping the noise level from 0.12 to 0.2. We note that at the low noise level, the overall performance starts to decrease at $l = 6$ and there does not exist a significant change in performance when it comes to the high noise, although $l = 4$ and $l = 5$ have a higher median. Figure 7(a) displays the overall short-term memory performance subject to low filter thresholds by grouping the threshold from 4 to 22 and Figure 7(b) displays the performance subject to high filter thresholds by grouping the threshold from 24 to 58. In both of them, we have witnessed a slight decrease in performance from $l = 6$. The cutting points of 'low' and 'high' in the above cases is chosen based on the patterns shown in Figure 12 and 13. However, if we investigate the performance subject to individual filter thresholds, it could look very different from what is shown in Figure 7. For instance, at

Preprints (www.preprints.org) | NOT PEER-REVIEWED | Posted: 9 August 2022 doi:10.20944/preprints202208.0170.v1

$f_0 = 46$ (Figure 8(b)) the best performance is achieved at $l = 7$ whilst with $f_0 = 18$ there is a decrease in performance after $l = 6$ which is similar to the overall result (Figure 7(a)). This demonstrates that different sizes of astrocytic coverage might optimize the performance at different spatial frequencies.

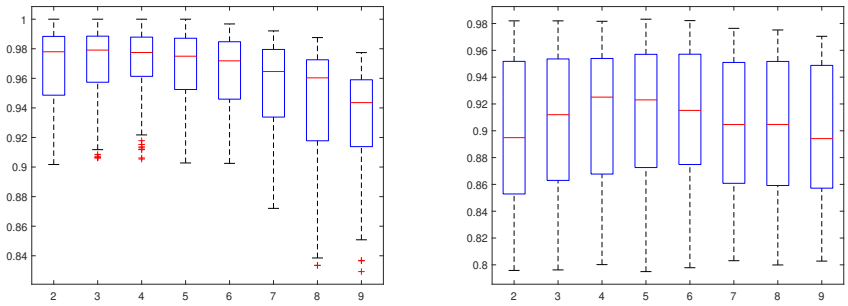

(a) Low noise (b) High noise

Figure 6. short-term memory performance subject to low and high salt-and-pepper noises. The horizontal axis denotes the size of astrocytic coverage and the vertical axis denotes the performance score.

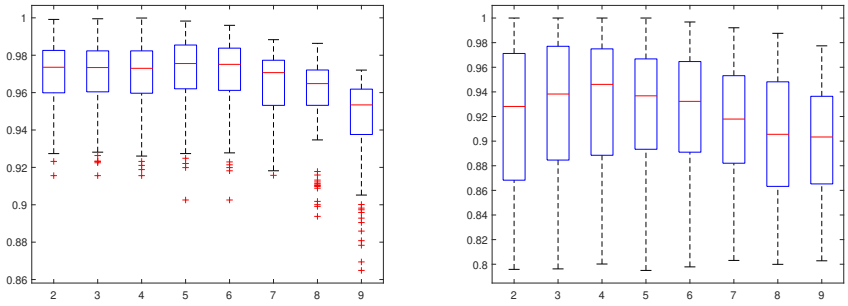

(a) Low-pass filter with low thresholds (b) Low-pass filter with high thresholds

Figure 7. short-term memory performance subject to low-pass filter with low and high thresholds. The horizontal axis denotes the size of astrocytic coverage and the vertical axis denotes the performance score.

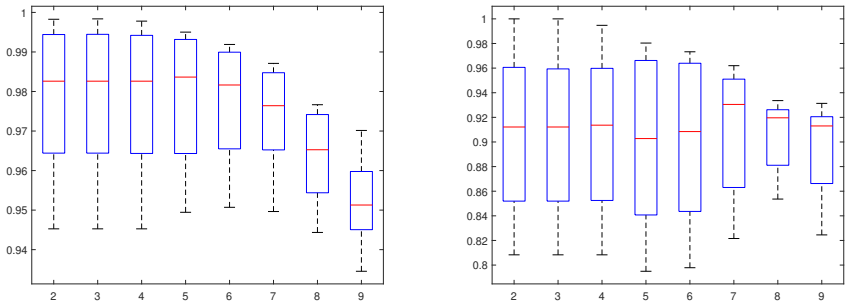

(a) $f_0 = 18$ (b) $f_0 = 46$

Figure 8. short-term memory performance subject to two individual filter thresholds. The horizontal axis denotes the size of astrocytic coverage and the vertical axis denotes the performance score.

Preprints (www.preprints.org) | NOT PEER-REVIEWED | Posted: 9 August 2022 doi:10.20944/preprints202208.0170.v1

We also observe that for a large astrocytic coverage, $l = 8$ for instance, a shorter time interval between training and testing tends to outperform a longer one when most of the frequency components have been included (Figure 9 right-end). Conversely, the performance barely changes with respect to a small astrocytic coverage such as $l = 4$ (Figure 10). For high filter thresholds, a longer time interval will result in more activated astrocytes as a result of calcium diffusion. However, a smaller astrocytic coverage has relatively little impact on the firing patterns of neurons at the testing stage because each astrocyte controls fewer neurons. Conversely, a bigger coverage will result in the over-firing of neurons in that more neurons that should not be activated have been activated, which decreases the performance. The above analysis is supported by the calcium patterns of astrocytes with different astrocytic coverage sizes and time intervals between training and testing shown in Figure 11. For relatively low filter thresholds, the firing pattern remains largely unchanged because of smoothing, as demonstrated previously.

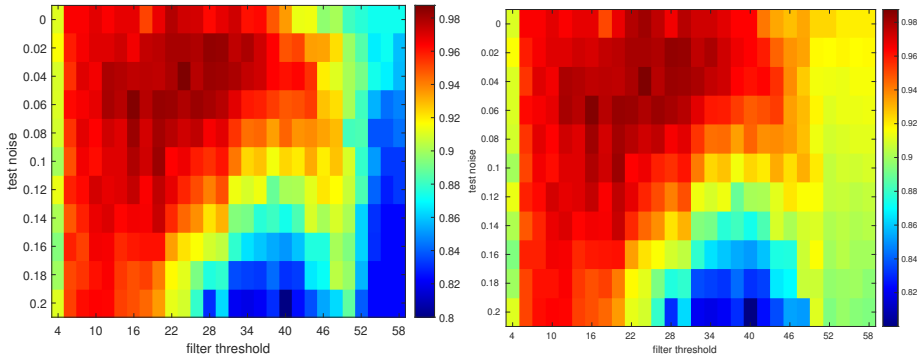

(a) $t_2 = 2$s, $t_e = 2.3$s (b) $t_2 = 1.5$s, $t_e = 1.8$s

Figure 9. The performance score C_p with different starting time t_2 with $l = 8$. In each sub-figure, the vertical axis denotes various levels of the salt-and-pepper noise at the testing stage. The horizontal axis denotes the threshold f_0 (increased by 2 units) of the low-pass filter.

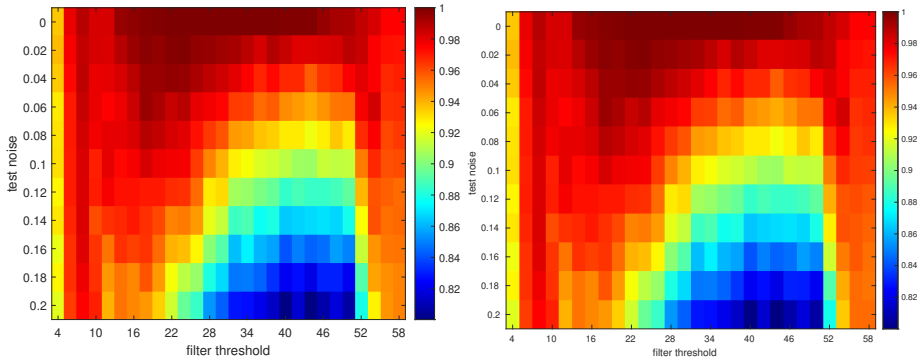

(a) $t_2 = 2$s, $t_e = 2.3$s (b) $t_2 = 1.5$s, $t_e = 1.8$s

Figure 10. The performance score C_p with different starting time t_2 with $l = 4$. In each sub-figure, the vertical axis denotes various levels of the salt-and-pepper noise at the testing stage. The horizontal axis denotes the threshold f_0 (increased by 2 units) of the low-pass filter.

Preprints (www.preprints.org) | NOT PEER-REVIEWED | Posted: 9 August 2022 doi:10.20944/preprints202208.0170.v1

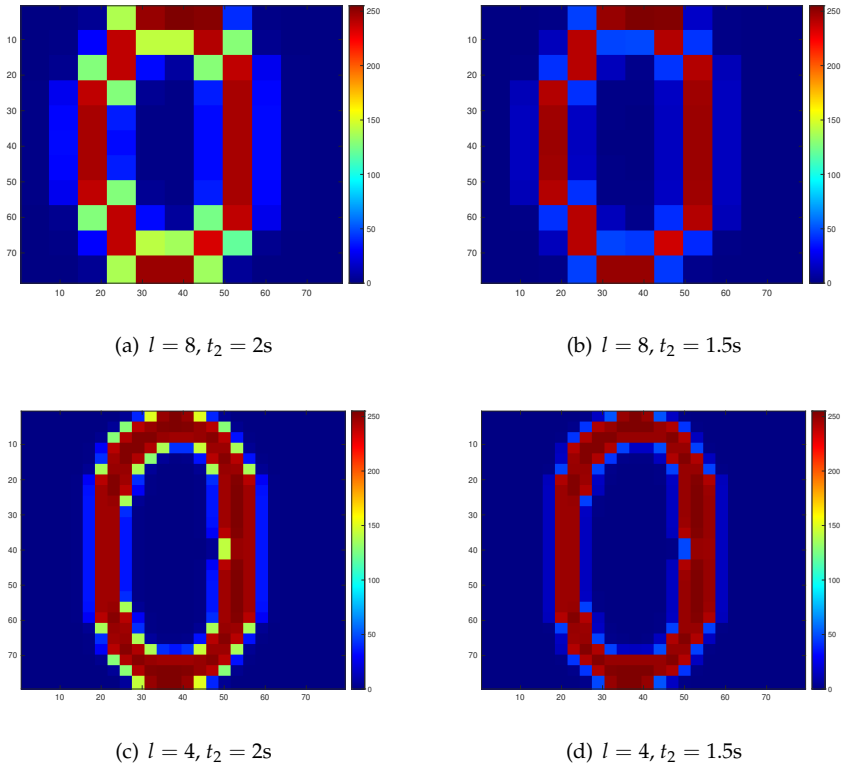

(a) $l = 8, t_2 = 2$s (b) $l = 8, t_2 = 1.5$s

(c) $l = 4, t_2 = 2$s (d) $l = 4, t_2 = 1.5$s

Figure 11. Calcium patterns of astrocytes with different astrocytic coverage areas and time intervals between training and testing. Here we use $f_0 = 58$ and noise level equal to 0.2 as an example.

4. Discussions

In light of the results shown in Figure 7, 8, 12 and 13, there are two hypotheses that may sound plausible:

1. Astrocytes may adjust their coverage areas in response to the change in spatial frequencies in order to optimize the short-term memory.
2. Different astrocytes may have different coverage areas in order to process different frequency components in order to optimize the short-term memory.

To the best of our knowledge, these open questions have not been given enough consideration yet and therefore, our work aims to raise the awareness of these plausible relations so that interested researchers may test and verify them in laboratory. Hypothesis 1 and 2 are not identical but they are somehow similar and could co-exist. As shown in Figure 7 and 8, although the majority of $l = 4$ outperforms $l = 7$, at some specific thresholds ($f_0 = 46$ for instance) $l = 7$ gives a slightly better performance. This may raise an open question for experimentalists to validate whether the astrocytes adjust their coverage areas in response to the changing spatial frequencies (hypothesis 1), or whether different astrocytes have different coverage areas (hypothesis 2), so as to assist the short-term memory. More precisely, it may be plausible to hypothesize that individual astrocytes are free to select from a wide range of coverage areas in order to optimally process the spatial information containing diverse frequency components; or at a particular time point, individual astrocytic modules, in which all astrocytes have identical coverage area, process some particular frequency components and hierarchically summarize the information to achieve the optimal short-term memory. In all, one is interpreted from a dynamic viewpoint and the other one from a static viewpoint, but they do not contradict with each other. The former one may also help to explain the findings that the astrocytic coverage of synapses is highly dynamic. Additionally, over the last decade, emerging evidence has shown that astrocytes actively participate in the brain energy mechanisms and potentially assist the energy-efficient coding of neuronal circuits [66–68]. It is reasonable to reckon that a

 doi:10.20944/preprints202208.0170.v1

compactly connected astrocytic network tend to consume more energy, therefore it seems plausible that a sparse layout could become more favorable so long as the precision is not considerably compromised. The results may provide a new perspective for those who study the roles played by astrocytes in cerebral energy-efficiency.

In regards to the small noise level, on the whole, a small astrocytic coverage tends to outperform a big one irrespective of the filter threshold. This may indirectly support the experimental result that the increasing density of astrocytes enhances short-term memory performances [40]. The comparison of $l = 2$, $l = 3$ and $l = 4$ also raises the potential to study whether over-crowded astrocytes will have negative effect on short-term memory for biologists.

As for the relatively high noise level, it appears that the performance score remains relatively low in a threshold interval and the more noisy the image is, the wider the interval is. We suppose the phenomenon is due to the fact that a higher salt-and-pepper noise distorts the original image more massively and the image decomposes into more frequency components (including many high frequencies). A relatively high filter threshold retains these frequencies (as a result of noise) which leads to a decrease in performance.

Finally, the sensitivity to the filter threshold also validates the necessity of introducing convolutional layers in spiking neural network for pattern recognition tasks because the idea of introducing filters is to extract the local patterns such as curves and straight lines.

One open question is whether the pattern displayed in Figure 12 will scale up with the size of the input image. Namely, when the size of the input is scaled up or down, whether the same pattern will be observed when the astrocytic coverage alters with the same ratio. This may shed light on the correspondence between the size of the input image and the astrocytic coverage.

In this work, we leveraged a computational neuron-astrocyte model for short-term memory that has been recently developed to study the impact of astrocytic coverage and spatial frequencies on short-term memory. We expect that the article can bring these unattended aspects to biologists' attention as a better understanding of this topic may pave the way for some transformative findings as to how neurons and glial cells adapt their behaviors in response to the external stimuli.

Preprints (www.preprints.org) | NOT PEER-REVIEWED | Posted: 9 August 2022 doi:10.20944/preprints202208.0170.v1

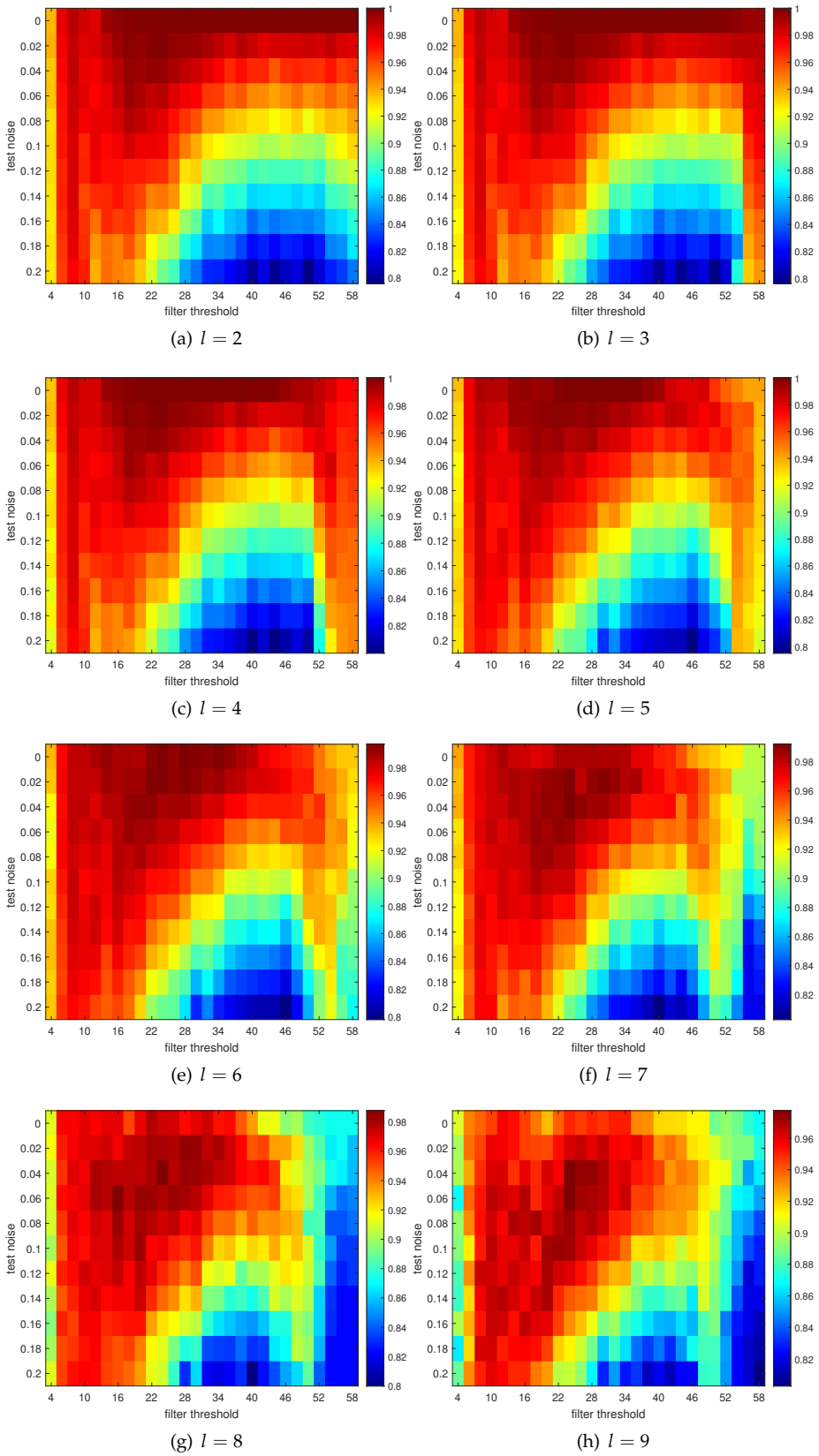

(a) $l = 2$ (b) $l = 3$

(c) $l = 4$ (d) $l = 5$

(e) $l = 6$ (f) $l = 7$

(g) $l = 8$ (h) $l = 9$

Figure 12. Performance score C_p for digit zero with various astrocytic coverage areas. In each sub-figure, the vertical axis denotes various levels of the salt-and-pepper noise at the testing stage. The horizontal axis denotes the threshold f_0 (increased by 2 units) of the low-pass filter.

Preprints (www.preprints.org) | NOT PEER-REVIEWED | Posted: 9 August 2022 doi:10.20944/preprints202208.0170.v1

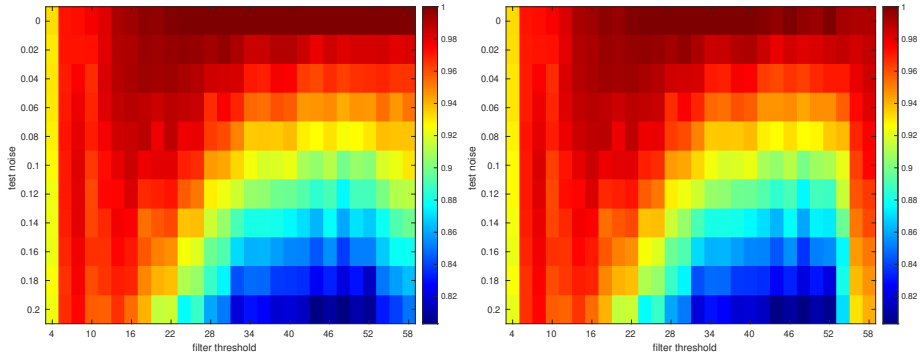

(a) $l = 2$

(b) $l = 3$

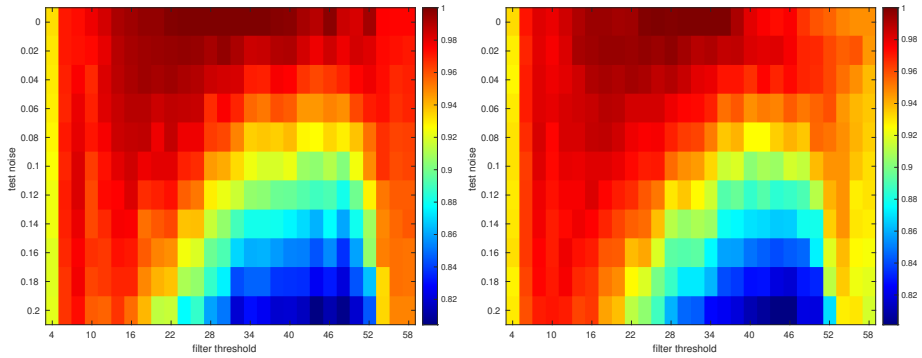

(c) $l = 4$

(d) $l = 5$

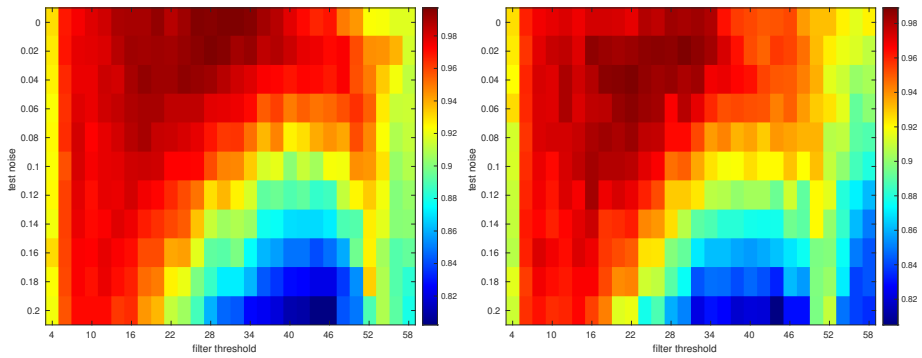

(e) $l = 6$

(f) $l = 7$

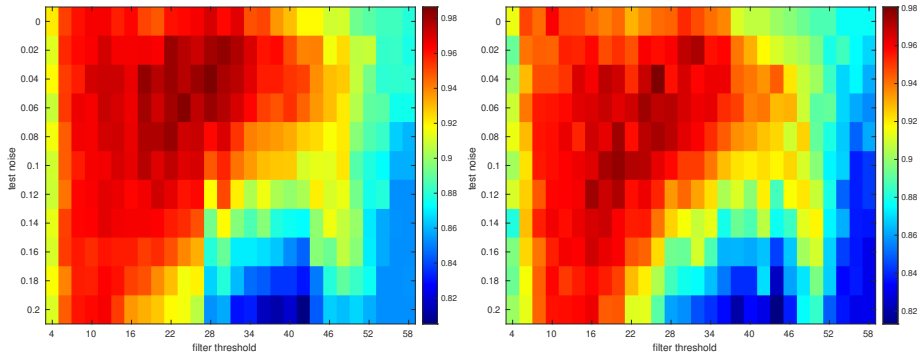

(g) $l = 8$

(h) $l = 9$

Figure 13. Performance score C_p for digit two with various astrocytic coverage areas. In each sub-figure, the vertical axis denotes various levels of the salt-and-pepper noise at the testing stage. The horizontal axis denotes the threshold f_0 (increased by 2 units) of the low-pass filter.

Author Contributions: Supervision: AZ; conceptualization: AZ and ZL; methods: SG and ZL; numerical simulation: YT and ZL; writing: ZL, AZ, SG, YT.

Funding: AZ and ZL thank UKRI Medical Research Council grant (MR/R02524X/1) and CRUK Early Detection Committee Project Award C12077/A26223, SG and YT thank Russian Science Foundation Grant No 22-12-00216.

Institutional Review Board Statement: Not applicable

Informed Consent Statement: Not applicable

Conflicts of Interest: The authors declare no conflict of interest.

References

1. Agulhon C, Petravicz J, McMullen AB, Sweger EJ, Minton SK, Taves SR, Casper KB, Fiacco TA, McCarthy KD. What is the role of astrocyte calcium in neurophysiology?. Neuron. 2008 Sep 25;59(6):932-46.
2. Booth HD, Hirst WD, Wade-Martins R. The role of astrocyte dysfunction in Parkinson's disease pathogenesis. Trends in neurosciences. 2017 Jun 1;40(6):358-70.
3. Upadhya R, Zingg W, Shetty S, Shetty AK. Astrocyte-derived extracellular vesicles: neuroreparative properties and role in the pathogenesis of neurodegenerative disorders. Journal of Controlled Release. 2020 Jul 10;323:225-39.
4. Rose CF, Verkhratsky A, Parpura V. Astrocyte glutamine synthetase: pivotal in health and disease. Biochemical Society Transactions. 2013 Dec 1;41(6):1518-24.
5. Brusilow SW, Koehler RC, Traystman RJ, Cooper AJ. Astrocyte glutamine synthetase: importance in hyperammonemic syndromes and potential target for therapy. Neurotherapeutics. 2010 Oct 1;7(4):452-70.
6. Gordleeva, S., Kanakov, O., Ivanchenko, M., Zaikin, A., Franceschi, C. Brain aging and garbage cleaning. Semin. Immunopathol. 42, 647–665. https://doi.org/10.1007/s00281-020-00816-x (2020).
7. Haydon PG. GLIA: listening and talking to the synapse. Nature Reviews Neuroscience. 2001 Mar;2(3):185-93.
8. Parpura V, Haydon PG. Physiological astrocytic calcium levels stimulate glutamate release to modulate adjacent neurons. Proceedings of the National Academy of Sciences. 2000 Jul 18;97(15):8629-34.
9. Araque A, Parpura V, Sanzgiri RP, Haydon PG. Tripartite synapses: glia, the unacknowledged partner. Trends in neurosciences. 1999 May 1;22(5):208-15.
10. Perea G, Araque A. GLIA modulates synaptic transmission. Brain research reviews. 2010 May 1;63(1-2):93-102.
11. Araque A, Parpura V, Sanzgiri RP, Haydon PG. Glutamate-dependent astrocyte modulation of synaptic transmission between cultured hippocampal neurons. European Journal of Neuroscience. 1998 Jun;10(6):2129-42.
12. Halassa MM, Fellin T, Haydon PG. The tripartite synapse: roles for gliotransmission in health and disease. Trends in molecular medicine. 2007 Feb 1;13(2):54-63.
13. Santello M, Calì C, Bezzi P. Gliotransmission and the tripartite synapse. Synaptic Plasticity. 2012:307-31.
14. Volterra A, Magistretti PJ, Haydon PG. The tripartite synapse: glia in synaptic transmission. Oxford University Press; 2002.
15. Perea G, Navarrete M, Araque A. Tripartite synapses: astrocytes process and control synaptic information. Trends in neurosciences. 2009 Aug 1;32(8):421-31.
16. Panatier A, Robitaille R. Astrocytic mGluR5 and the tripartite synapse. Neuroscience. 2016 May 26;323:29-34.
17. Fellin T, Pascual O, Gobbo S, Pozzan T, Haydon PG, Carmignoto G. Neuronal synchrony mediated by astrocytic glutamate through activation of extrasynaptic NMDA receptors. Neuron. 2004 Sep 2;43(5):729-43.
18. Allegrini P, Fronzoni L, Pirino D. The influence of the astrocyte field on neuronal dynamics and synchronization. Journal of biological physics. 2009 Oct;35(4):413-23.
19. Wade JJ, McDaid LJ, Harkin J, Crunelli V, Kelso JS. Bidirectional coupling between astrocytes and neurons mediates learning and dynamic coordination in the brain: a multiple modeling approach. PloS one. 2011 Dec 29;6(12):e29445.
20. Pankratova EV, Kalyakulina AI, Stasenko SV, Gordleeva SY, Lazarevich IA, Kazantsev VB. Neuronal synchronization enhanced by neuron–astrocyte interaction. Nonlinear Dynamics. 2019 Jul;97(1):647-62.
21. Gordleeva SY, Ermolaeva AV, Kastalskiy IA, Kazantsev VB. Astrocyte as spatiotemporal integrating detector of neuronal activity. Frontiers in physiology. 2019 Apr 18;10:294.
22. Chen N, Sugihara H, Sharma J, Perea G, Petravicz J, Le C, Sur M. Nucleus basalis-enabled stimulus-specific plasticity in the visual cortex is mediated by astrocytes. Proceedings of the National Academy of Sciences. 2012 Oct 9;109(41):E2832-41.
23. Gordleeva S, Tsybina YA, Krivonosov MI, Tyukin IY, Kazantsev VB, Zaikin AA, Gorban AN. Situation-based memory in spiking neuron-astrocyte network. arXiv preprint arXiv:2202.07218. 2022 Feb 15.
24. Tsybina Y, Gordleeva S, Krivonosov M, Kastalskiy I, Zaikin A, Gorban A. Modelling working memory in neuron-astrocyte network. In2021 International Joint Conference on Neural Networks (IJCNN) 2021 Jul 18 (pp. 1-6). IEEE.
25. Gordleeva SY, Tsybina YA, Krivonosov MI, Ivanchenko MV, Zaikin AA, Kazantsev VB, Gorban AN. Modelling working memory in spiking neuron network accompanied by astrocytes. Frontiers in Cellular Neuroscience. 2021;15:86.
26. Tsybina Y, Kastalskiy I, Krivonosov M, Zaikin A, Kazantsev V, Gorban A, Gordleeva S. Astrocytes mediate analogous memory in a multi-layer neuron-astrocytic network. Neural Comput. Appl. 2022

 doi:10.20944/preprints202208.0170.v1

27. Tsybina Y, Krivonosov M, Gordleeva S, Zaikin A, Gorban A. Short-term memory in neuron-astrocyte network. In2020 4th Scientific School on Dynamics of Complex Networks and their Application in Intellectual Robotics (DCNAIR) 2020 Sep 7 (pp. 245-247). IEEE.
28. Kastalskiy I, Tsybina Y, Kazantsev V, Gordleeva S. Astrocytes' signals guided storage and retrieval of patterns by an SNN. In2021 Third International Conference Neurotechnologies and Neurointerfaces (CNN) 2021 Sep 13 (pp. 34-37). IEEE.
29. Makovkin, S., Kozinov, E., Ivanchenko, M. et al. Controlling synchronization of gamma oscillations by astrocytic modulation in a model hippocampal neural network. Sci Rep 12, 6970 (2022).
30. Makovkin, S. Y., Shkerin, I. V., Gordleeva, S. Y., Ivanchenko, M. V. Astrocyte-induced intermittent synchronization of neurons in a minimal network. Chaos Solitons Fractals 138, 109951.
31. Gordleeva, S. Y., Lebedev, S. A., Rumyantseva, M. A., Kazantsev, V. B. Astrocyte as a detector of synchronous events of a neural network. JETP Lett. 107, 440–445.
32. Abrego L, Gordleeva S, Kanakov O, Krivonosov M, Zaikin A. Estimating integrated information in bidirectional neuron-astrocyte communication. Physical Review E. 2021 Feb 19;103(2):022410.
33. Kanakov O, Gordleeva S, Ermolaeva A, Jalan S, Zaikin A. Astrocyte-induced positive integrated information in neuron-astrocyte ensembles. Physical Review E. 2019 Jan 23;99(1):012418.
34. Abrego Rangel LA. Information processing in biological complex systems: a view to bacterial and neural complexity (Doctoral dissertation, UCL (University College London)).
35. Kanakov O, Gordleeva S, Zaikin A. Integrated Information in the Spiking–Bursting Stochastic Model. Entropy. 2020 Dec;22(12):1334.
36. Suzuki A, Stern SA, Bozdagi O, Huntley GW, Walker RH, Magistretti PJ, Alberini CM. Astrocyte-neuron lactate transport is required for long-term memory formation. Cell. 2011 Mar 4;144(5):810-23.
37. Habbas S, Santello M, Becker D, Stubbe H, Zappia G, Liaudet N, Klaus FR, Kollias G, Fontana A, Pryce CR, Suter T. Neuroinflammatory TNFα impairs memory via astrocyte signaling. Cell. 2015 Dec 17;163(7):1730-41.
38. Adamsky A, Kol A, Kreisel T, Doron A, Ozeri-Engelhard N, Melcer T, Refaeli R, Horn H, Regev L, Groysman M, London M. Astrocytic activation generates de novo neuronal potentiation and memory enhancement. Cell. 2018 Jun 28;174(1):59-71.
39. Kozachkov L, Michmizos KP. Sequence Learning in Associative Neuronal-Astrocytic Networks. InInternational Conference on Brain Informatics 2020 Sep 19 (pp. 349-360). Springer, Cham.
40. De Luca SN, Soch A, Sominsky L, Nguyen TX, Bosakhar A, Spencer SJ. Glial remodeling enhances short-term memory performance in Wistar rats. Journal of neuroinflammation. 2020 Dec;17(1):1-8.
41. Cowan N. Working memory underpins cognitive development, learning, and education. Educational psychology review. 2014 Jun 1;26(2):197-223.
42. Baddeley A. Working memory: The interface between memory and cognition. Journal of cognitive neuroscience. 1992 Jul 1;4(3):281-8.
43. Nairne JS. Short-term/working memory. InMemory 1996 Jan 1 (pp. 101-126). Academic Press.
44. Lima A, Sardinha VM, Oliveira AF, Reis M, Mota C, Silva MA, Marques F, Cerqueira JJ, Pinto L, Sousa N, Oliveira JF. Astrocyte pathology in the prefrontal cortex impairs the cognitive function of rats. Molecular psychiatry. 2014 Jul;19(7):834-41.
45. Robin LM, da Cruz JF, Langlais VC, Martin-Fernandez M, Metna-Laurent M, Busquets-Garcia A, Bellocchio L, Soria-Gomez E, Papouin T, Varilh M, Sherwood MW. Astroglial CB1 receptors determine synaptic D-serine availability to enable recognition memory. Neuron. 2018 Jun 6;98(5):935-44.
46. Santello M, Toni N, Volterra A. Astrocyte function from information processing to cognition and cognitive impairment. Nature neuroscience. 2019 Feb;22(2):154-66.
47. Akther S, Hirase H. Assessment of astrocytes as a mediator of memory and learning in rodents. Glia. 2021 Sep 28.
48. Chung WS, Allen NJ, Eroglu C. Astrocytes control synapse formation, function, and elimination. Cold Spring Harbor perspectives in biology. 2015 Sep 1;7(9):a020370.
49. Heller JP, Rusakov DA. Morphological plasticity of astroglia: understanding synaptic microenvironment. Glia. 2015 Dec;63(12):2133-51.
50. Rusakov DA. Disentangling calcium-driven astrocyte physiology. Nature Reviews Neuroscience. 2015 Apr;16(4):226-33.
51. Tanaka M, Shih PY, Gomi H, Yoshida T, Nakai J, Ando R, Furuichi T, Mikoshiba K, Semyanov A, Itohara S. Astrocytic Ca 2+ signals are required for the functional integrity of tripartite synapses. Molecular brain. 2013 Dec;6(1):1-3.
52. Wu YW, Tang X, Arizono M, Bannai H, Shih PY, Dembitskaya Y, Kazantsev V, Tanaka M, Itohara S, Mikoshiba K, Semyanov A. Spatiotemporal calcium dynamics in single astrocytes and its modulation by neuronal activity. Cell calcium. 2014 Feb 1;55(2):119-29.
53. Kustikova V, Krivonosov M, Pimashkin A, Denisov P, Zaikin A, Ivanchenko M, Meyerov I, Semyanov A. CalciumCV: Computer vision software for calcium signaling in astrocytes. InInternational Conference on Analysis of Images, Social Networks and Texts 2018 Jul 5 (pp. 168-179). Springer, Cham.
54. Matrosov, V. et al. Emergence of regular and complex calcium oscillations by inositol 1, 4, 5-trisphosphate signaling in astrocytes. In Springer Series in Computational Neuroscience 151–176 (Springer International Publishing, 2019).
55. Izhikevich EM. Simple model of spiking neurons. IEEE Transactions on neural networks. 2003 Nov;14(6):1569-72.

56. Kazantsev VB, Asatryan SY. Bistability induces episodic spike communication by inhibitory neurons in neuronal networks. Physical Review E. 2011 Sep 13;84(3):031913.
57. Kazantsev, V., Gordleeva, S., Stasenko, S. Dityatev, A. A homeostatic model of neuronal fring governed by feedback signals from the extracellular matrix. PLoS ONE. 2012 7, e41646.
58. Gordleeva SY, Stasenko SV, Semyanov AV, Dityatev AE, Kazantsev VB. Bi-directional astrocytic regulation of neuronal activity within a network. Frontiers in computational neuroscience. 2012 Nov 2;6:92.
59. Berridge MJ. The inositol trisphosphate/calcium signaling pathway in health and disease. Physiological reviews. 2016 Oct;96(4):1261-96.
60. Berridge MJ. Inositol trisphosphate and calcium signalling. Nature. 1993 Jan;361(6410):315-25.
61. Nadkarni S, Jung P. Modeling synaptic transmission of the tripartite synapse. Physical biology. 2007 Jan 9;4(1):1.
62. Oschmann F, Berry H, Obermayer K, Lenk K. From in silico astrocyte cell models to neuron-astrocyte network models: A review. Brain research bulletin. 2018 Jan 1;136:76-84.
63. Liu L, Gao H, Zaikin A, Chen S. Unraveling Aβ-Mediated Multi-Pathway Calcium Dynamics in Astrocytes: Implications for Alzheimer's Disease Treatment From Simulations. Frontiers in physiology. 2021;12.
64. Yu-Wei Wu,Susan Gordleeva,Xiaofang Tang,Pei-Yu Shih,Yulia Dembitskaya,Alexey Semyanov. Morphological profile determines the frequency of spontaneous calcium events in astrocytic processes. Glia. 2019; 67(2):246-262.
65. Ullah G, Jung P, Cornell-Bell AH. Anti-phase calcium oscillations in astrocytes via inositol (1, 4, 5)-trisphosphate regeneration. Cell calcium. 2006 Mar 1;39(3):197-208.
66. Belanger M, Allaman I, Magistretti PJ. Brain energy metabolism: focus on astrocyte-neuron metabolic cooperation. Cell metabolism. 2011 Dec 7;14(6):724-38.
67. Stobart JL, Anderson CM. Multifunctional role of astrocytes as gatekeepers of neuronal energy supply. Frontiers in cellular neuroscience. 2013 Apr 10;7:38.
68. Kastanenka KV, Moreno-Bote R, De Pittà M, Perea G, Eraso-Pichot A, Masgrau R, Poskanzer KE, Galea E. A roadmap to integrate astrocytes into Systems Neuroscience. Glia. 2020 Jan;68(1):5-26.